JOURNAL OF CATALYSIS 107, 114–128 (1987)

An Integrated Study of $Pt/WO_3/SiO_2$ Catalysts for the NO–CO Reaction

I. Catalyst Characterization by XRD, Chemisorption, and XPS

J. R. REGALBUTO,[1] T. H. FLEISCH,* E. E. WOLF†,[2]

†*Department of Chemical Engineering, University of Notre Dame, Notre Dame, Indiana 46556; and* **Amoco Research Center, Naperville, Illinois 60566*

Received October 23, 1986; revised March 12, 1987

$Pt/WO_3/SiO_2$ catalysts were characterized by X-ray diffraction (XRD), selective CO chemisorption, and X-ray photoelectron spectroscopy (XPS). It was found that the presence of WO_3 decreased final Pt crystallite size, in part by reducing the formation of bulk $PtCl_2$ precursor. However, CO chemisorption was suppressed; this indicated strong metal-promoter interactions. Changes in Pt electron binding energy suggest that charge transfer may also take place. A model of the surface consisting of Pt crystallites decorated by partially reduced WO_x is proposed. This morphological model was supported by XRD and XPS results which revealed a surface-localized phase of partially reduced WO_x (likely WO_2). Decoration was also indicated in the trend of XPS Pt/Si ratios.

INTRODUCTION

In automotive catalysis, it is desirable to promote the activity of noble metals with less expensive metals or metal oxides. In previous work this group has investigated the activity of $Pt–Cu/SiO_2$ (*1, 2*), and $Pt–Cr_2O_3/SiO_2$ (*3*) for CO oxidation. The present investigation focuses on the promotional mechanism of tungsta in supported Pt catalysts for the NO–CO reaction. The trioxides of tungsten and molybdenum are the most recent promoters studied for automotive pollution control catalysis (*4–8*).

The choice of a tungsten promoter for Pt is attractive in that elemental tungsten displays high NO dissociation activity (*9–12*) which could compensate for the low dissociation activity of Pt. Once dissociated, however, adatoms of N and O are very strongly bound to the W surface. TPD studies on polycrystalline W have shown that N_2 desorbs above 1000°C and O_2 at even higher temperatures (*9*). Consequently W by itself has not proven useful as an NO dissociation catalyst (*10*). Furthermore, in an oxidizing environment, the trioxide form (tungsta or WO_3) is the stable form. Bulk unsupported tungsta does not reduce below 427°C and supported tungsta becomes even more difficult to reduce (*13, 14*).

The drawbacks of W toward NO dissociation might be overcome if it is combined in close contact with a noble metal such as Pt. It has been shown that partial reduction in tungsta by Pt occurs via hydrogen spillover to yield hydrogen tungsten bronzes (HTBs) (*15–18*). Furthermore, Pt sites in close proximity to partially reduced tungsta sites might promote the removal of N and O adatoms from these sites via the so-called porthole effect (*15*). Such close proximity should be created by sequential impregnation of tungsta and Pt followed by reduction.

The combination of a partially reducible oxide with a noble metal can result in strong metal support interactions (SMSI) as has been reported for Pt, Rh, and Ni supported on TiO_2 and other partially reducible

[1] Present address: Department of Chemical Engineering, University of Illinois at Chicago, Box 4348, Chicago, IL 60680.

[2] To whom correspondence should be addressed.

0021-9517/87 $3.00

oxides (*19*). Very recently, this state has been suggested for a Re/WO_3/activated carbon catalyst (*20*). Of interest in the present study is to determine, among other effects, whether chemisorption suppression and SMSI morphology indeed occur in silica-supported catalysts containing Pt and tungsta. SMSI-type behavior has been reported for TiO_2–SiO_2 containing catalysts of Rh (*24, 25*), and Pt and Ir (*26*), but was not reported in work on alumina-supported Pt/MoO_3 (*4–6*) and Pd/WO_3 (*7, 8*) or silica-supported Pd/La_2O_3 (*27*).

The promotional effect on WO_3 on Pt/SiO_2 catalysts for the NO–CO reaction was evaluated in an integral manner, by turning attention first to characterization of the promoted catalysts and then to the influence of the promoter on the kinetics and reaction mechanism. In this first work, catalyst characterization was accomplished by a multifaceted approach including X-ray diffraction (XRD), X-ray photoelectron spectroscopy (XPS), and selective chemisorption. In the second (*21*), catalyst morphology as a function of pretreatment was monitored using transmission electron microscopy (TEM). In the third work the NO–CO reaction kinetics and mechanism over the promoted and unpromoted catalysts is studied with transmission Fourier transform infrared (FTIR) spectroscopy (*22*). These studies have been integrated by the successful correlation of kinetic, mechanistic, and characterization results (*22, 23*).

EXPERIMENTAL

Catalysts

In order to fully investigate the behavior of both WO_3 and Pt in $Pt/WO_3/SiO_2$ catalysts, three catalyst series were used, with Pt and WO_3 compositions as given in Table 1. These three series will be referred to as tungsta free (Pt/SiO_2), low tungsta loading ($Pt/WO_3/SiO_2$), and high tungsta loading (Pt/WO_3–SiO_2). Using the higher tungsta loading permitted a clearer illustration of the influence of WO_3 on Pt morphology, and a better characterization of WO_3. The observations of the partial reduction in WO_3 by its chromatic effect (pale yellow WO_3 turns into a dark blue HTB), by XPS (W^{+5} formation), and also by X-ray diffraction were made possible because small crystallites of bulk WO_3 were formed in the high tungsta catalysts.

TABLE 1

Catalyst Compositions[a] and Designations

Tungsta free Pt/SiO_2[b]	Low tungsta $Pt/WO_3/SiO_2$[b]	High tungsta Pt/WO_3–SiO_2[b]
	6.2 WO_3/SiO_2	25 WO_3/SiO_2
1.2 Pt/SiO_2	1.2 Pt/4.7 WO_3/SiO_2	1.2 Pt/25 WO_3–SiO_2
2.5 Pt/SiO_2	2.5 Pt/3.2 WO_3/SiO_2	2.5 Pt/25 WO_3–SiO_2
3.8 Pt/SiO_2	3.8 Pt/1.7 WO_3/SiO_2	3.8 Pt/25 WO_3–SiO_2
5.0 Pt/SiO_2	—	5.0 Pt/25 WO_3–SiO_2

[a] The number preceding the catalytic component represents its composition in weight percent.
[b] General designation for each catalyst series.

The catalysts were formulated using a high surface area silica (Harshaw, 600 m^2/g), chloroplatinic acid (Mallinckrodt), and anhydrous ammonium tungstate, AAT ($(NH_4)_2WO_4$, Aldrich), or ammonium metatungstate, AMT ($(NH_4)_6H_2W_{12}O_{49} \cdot 4H_2O$, Climax Molybdenum Co.). The AMT was used for the high WO_3 loading series since it is soluble in water at the required concentration, while AAT is not.

The WO_3 free series of 1.2, 2.5, 3.8, and 5.0 wt% Pt/SiO_2 catalysts was prepared by impregnation of chloroplatinic acid to incipient wetness of the silica gel, followed by vacuum-drying at 80°C for 2 hr, 300°C calcination in air for 3 hr, and 425°C reduction in 95% H_2–5% He for 3 hr. The second series of catalysts, the low tungsta loading series, contained a total of 5 wt% metal (Pt + W) and varying Pt and WO_3 ratios as shown in Table 1. The support was first impregnated with an aqueous solution of AAT, followed by the same Pt impregnation procedure as that described above. The first impregnation was followed by vacuum-drying at 80°C for 2 hr, and calcination at 700°C for 3 hr to ensure complete oxidation of tung-

sten. The same sequential impregnation was used for the high tungsta loading catalysts, using instead an aqueous AMT solution to produce 25 wt% WO_3.

Catalyst Characterization

X-ray diffraction. The Diano XPG 2 X-ray diffractometer employed for catalyst characterization was equipped with a Cu source (Cu$K\alpha$ radiation) and a graphite monochromator. A 3° beam slit and 0.2° detector slit were used. Standard source voltage and amperage were 45 kV and 30 mA. Because of the relatively low loadings of Pt and WO_3, the crystalline components of interest, the scan rate was usually set at 0.5°/min. A detector time constant (T_c) of 10 s was best suited to this rate. Diffraction patterns were recorded continuously on a strip chart recorder. In all the XRD work the above parameters remained unchanged.

Samples of catalyst powder were pressed into wafers and affixed to standard-sized glass microscope slides using double-sided tape. The samples were approximately 2 cm by 3 cm in area, and about 0.5 mm thick. A 5 wt% Pt standard sample was prepared to obtain a measure of both instrumental broadening and broadening due to the sampling depth. The standard consisted of Pt filings which had been annealed in N_2 at 800°C for 2 hr to remove any residual stress induced by the filing. These were physically mixed with SiO_2 powder and pressed into a wafer using the same pressure as was used for the real catalyst samples. The resulting broadening due to instrumental and depth factors was 0.330° (*20*).

Diffraction patterns of each of the catalyst compositions were obtained at all steps of preparation. To do so, powder was withdrawn from each catalyst lot after each preparation step; the lots were exposed to air at room temperature between treatments. Calculations for average crystallite size were made using Pt (111) linewidths in Scherrer's equation, with the Gaussian lineshape approximation.

Chemisorption. Infrared results (*22*) indicated that CO adsorbs preferentially on Pt in Pt/WO_3 catalysts. No CO chemisorption was detected in Pt free catalysts. Consequently selective CO chemisorption was used to estimate Pt surface area.

A dynamic flow method was employed using CO in a helium carrier. Approximately 600 mg of a catalyst sample was placed in the reactor of a flow system which could be switched between pretreatment and chemisorption functions. Gases employed for pretreatment were ultrahigh purity H_2 and He and CP grade O_2 (Linde). The He carrier gas was further purified by two high capacity Alltech Oxy-traps in series, one just after the He cylinder and the other just before the sample loop valve. The chemisorption gas was a 10% CO in He mixture (CP grade, Linde). Dispersion was calculated assuming a 1 : 1 chemisorption stoichiometry between CO and Pt sites, and average crystallite sizes were calculated assuming hemispherical geometry. IR data indicate that in the presence of gas phase CO, the only detectable species is linear CO adsorbed on Pt. Hence the 1 : 1 stoichiometry is justified and assumed to be independent of crystallite size. Adsorbate loss was checked by pulsing additional CO up 15 min after saturation, and it was found to be less than 5% of the total uptake.

X-ray photoelectron spectroscopy. XPS was performed at the Amoco Research Center in Naperville, Illinois. The Hewlett–Packard 5950 XPS spectrometer employed operated with a monochromated aluminum source producing Al$K\alpha$ radiation with 1486.6 eV. A full width at half-maximum (FWHM) of 0.9 eV is typically achieved for the Au $4f_{7/2}$ line. An electron flood gun providing low energy electrons (<10 eV) was used to minimize sample charging. The instrument was equipped with *in situ* treatment chambers where samples can be reacted in flowing UHP gases at 1 atm and up to 1000°C before they are transferred under UHV to the analysis chamber. Sample wafers were pressed from approximately 50 mg of catalyst powder. A more detailed de-

scription of this apparatus is given elsewhere (*28*).

Catalysts were scanned for Pt (Pt 4*f*, 73–71 eV), W (W 4*f*, 33–36 eV), Cl (Cl 2*p*, 198–200 eV), Si (Si 2*p*, 103–105 eV), and O (O 1*s*, 532–533 eV) before and after reduction. The Si 2*p* electron binding energy (ebe) at 103.5 eV was used as reference and gives reproducible results to ±0.1 eV. This reference was found to yield more reproducible ebes than the more commonly used C 1*s* at 284.6 eV reference. Because W exhibited multiple oxidation states in the final, reduced state, the relative amounts of the various oxidation states were quantitatively deconvoluted from the experimental curves using a standard Gaussian peak-fitting routine. The well-known spin-orbit split and the theoretical $4f_{7/2}/4f_{5/2}$ area ratios were kept constant in the peak-fit routine to assure a quantitative deconvolution. Quantitative calculations of surface compositions were performed in a conventional manner described elsewhere (*32*). The Pt/Si ratio was used as a measure of dispersion which complemented measurements by the other techniques.

RESULTS

BET surface area and chromatic effects. The two tungsta-containing catalyst series were formulated such that WO_3 would be present in a highly dispersed form in the low loading series, and partly present as bulk WO_3 in the high loading series. The breakpoint concentration, i.e., the maximum concentration for monolayer formation beyond which bulk WO_3 also forms, has been estimated to be 1 atom W/nm^2 (*14*). Using the manufacturer's surface area of the support of 600 m^2/g, this concentration corresponds to a bulk loading of 23.2%. BET surface areas for the SiO_2 support and reduced catalysts of all three series are given in Table 2 and reveal that surface area decreased rapidly with the addition of WO_3. However, surface area changed little if at all with addition of Pt.

Upon reduction, the chromatic effect corresponding to the formation of HTB was observed very readily for the high tungsta catalysts. The Pt free, high tungsta catalysts were pale yellow after calcination and remained so when reduced at temperatures up to and including 400°C. Reduction at 425°C resulted in a dark blue color. The high tungsta, Pt-containing catalysts reduced to a black color at 400°C. The blue and black forms appeared very stable; the intensity of the blue and black colors remained constant after several months of storage in air at room temperature, as well as after a 1-hr treatment in He at 400°C. The chromatic effect was not as readily observable for the low tungsta catalysts. Immediately after reduction their brown coloration was initially darker than that for the corresponding tungsta free catalysts, but their intensity faded with storage in air at room temperature. The fully reduced (as verified by XRD and XPS) tungsta free catalysts were all light brown and the brown intensity increased slightly with Pt loading.

TABLE 2

BET Surface Area Versus Tungsta Loading

Catalyst composition	BET surface area (m^2/g SiO_2)
SiO_2	630
1.2 Pt/SiO_2	610
5.0 Pt/SiO_2	610
1.2 Pt/4.7 WO_3/SiO_2	588
1.2 Pt/25 WO_3–SiO_2	434
3.8 Pt/25 WO_3–SiO_2	420

X-ray diffraction. In Fig. 1 the X-ray diffraction patterns of the different colors and forms of WO_3 in the high tungsta loading catalysts are compared. The Pt free, yellow form exhibited the expected monoclinic pattern of fully oxidized WO_3 (*29*). The blue hydrogen tungsten bronze form was produced from this Pt free sample by a reduction at 425°C, and was identified as either a rhombic or a cubic hydrogen tungsten bronze (*29*). The most notable of the differences in the diffraction patterns of mono-

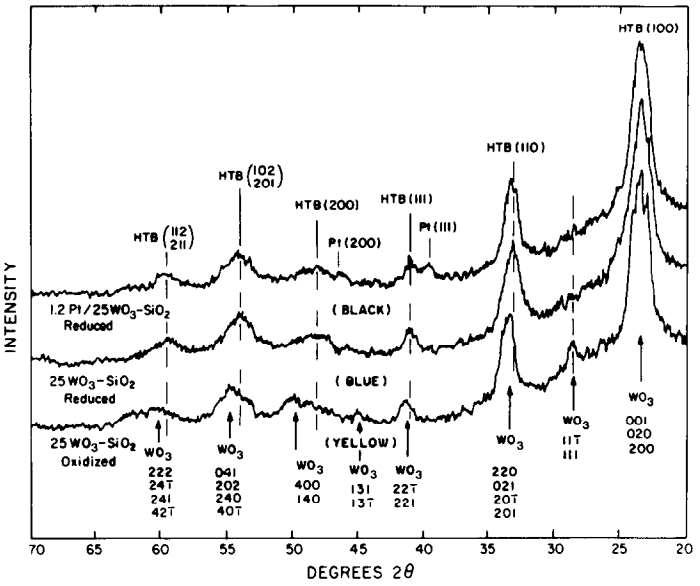

FIG. 1. XRD patterns of fully oxidized (yellow), and reduced (blue) 25 WO_3–SiO_2 supports, and a partially reduced 1.2 Pt/25 WO_3–SiO_2 catalyst showing lines corresponding to hydrogen tungsten bronzes.

clinic WO_3 and the HTB are the conglomeration of the (001), (200), and (020) WO_3 peaks centered at $2\theta = 24.5°$ into the HTB (100) peak, the disappearance of the WO_3 (111) peaks at 27.4 degrees, and various other peak shifts as indicated in the figure. The diffraction patterns of the rhombic ($H_{0.33}WO_3$) and cubic ($H_{0.5}WO_3$) forms are very similar (*29*) and their differentiation was further hindered by peak broadening, so that the exact composition of the HTBs could not be determined.

The XRD pattern of the black form, containing 1.2 wt% Pt and reduced at 400°C, exhibited virtually the same peaks as the blue form and additionally unshifted Pt peaks at $2\theta = 39.7$ and 46.5°. In spite of the difference in color, then, bulk WO_3 in the Pt-containing catalysts is in the form of HTB.

The crystallographic composition of Pt-containing phases was also studied as a function of pretreatment, beginning with the impregnation and drying step. The tungsta free and low tungsta catalysts showed no appreciable crystallinity at this stage, while the high tungsta series displayed peaks corresponding to monoclinic, fully oxidized WO_3. This bulk WO_3 phase had formed upon the initial 700°C calcination and displayed no change through the Pt impregnation and drying step.

The crystallographic changes induced by the second (300°C) calcination, after reimpregnation and drying of chloroplatinic acid, are revealed in Fig. 2. $PtCl_2$ was observed in all catalyst series, exhibiting main peaks at $2\theta = 13.6$, 30.3, and 35.5°. This was the only crystalline phase detected in the tungsta free and low tungsta series (Figs. 2A and 2B). In addition to $PtCl_2$, monoclinic WO_3 was again observed for the high tungsta series (Fig. 2C) and was unchanged by the second calcination. In each series, $PtCl_2$ peaks broadened with increasing WO_3 loading, most clearly seen for the $PtCl_2$ peaks at $2\theta = 13.6$ and 35.5°, proceeding from Fig. 2A to 2C.

X-ray diffraction patterns which illustrate the formation of Pt crystallites upon reduction and the trend in Pt peak broadening with increasing tungsta loading are

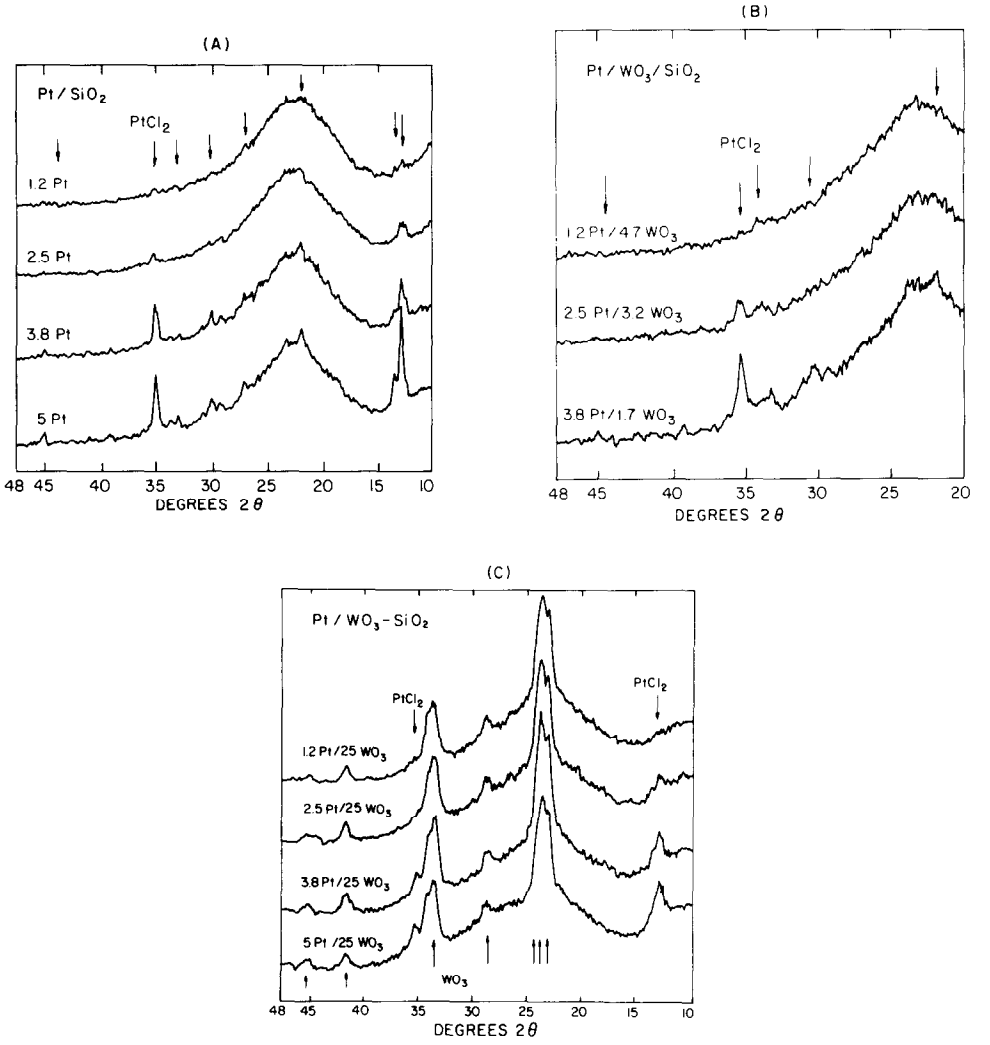

FIG. 2. XRD patterns of the calcined (A) WO_3 free, (B) low tungsta, and (C) high tungsta catalysts at various Pt loadings showing lines corresponding to $PtCl_2$ and WO_3.

shown in Fig. 3. Pt peaks were observed in the normal face-centered cubic (fcc) pattern of metallic Pt, at $2\theta = 39.8°$ (111) and $2\theta = 46.5°$ (200), for all series. Pt peaks were the only peaks observed for the tungsta free and low tungsta series (Figs. 3A and 3B), while HTB peaks were present in the high tungsta series (Fig. 3C). The unshifted position of all Pt peaks indicated that Pt forms a separate phase from the HTB.

Comparing the low tungsta catalysts (Fig. 3B) to the tungsta free catalysts (Fig. 3A), one sees that Pt peaks display broadening proportional to the amount of WO_3 present; broadening was so great for the $1.2Pt/4.7WO_3$ catalyst that the Pt peaks were not observed. In the high tungsta series (Fig. 3C) the peaks of even the high Pt loading catalysts exhibited considerable broadening. A peak also appeared, however, for the 1.2 wt% Pt catalyst. This catalyst was the only exception to the trend of increasing peak broadening with increased WO_3 loading. If estimates of Pt crystallite size are valid in spite of the 50-Å detection limit of the X-ray diffractometer, then Pt

crystallite size in the final, reduced state appeared to decrease with increased WO_3 loading.

Average Pt crystallite sizes were calculated from these patterns using the Pt (111) peaks and are compared to those sizes calculated from chemisorption data in Fig. 5.

Chemisorption. Infrared data (*22*) re-

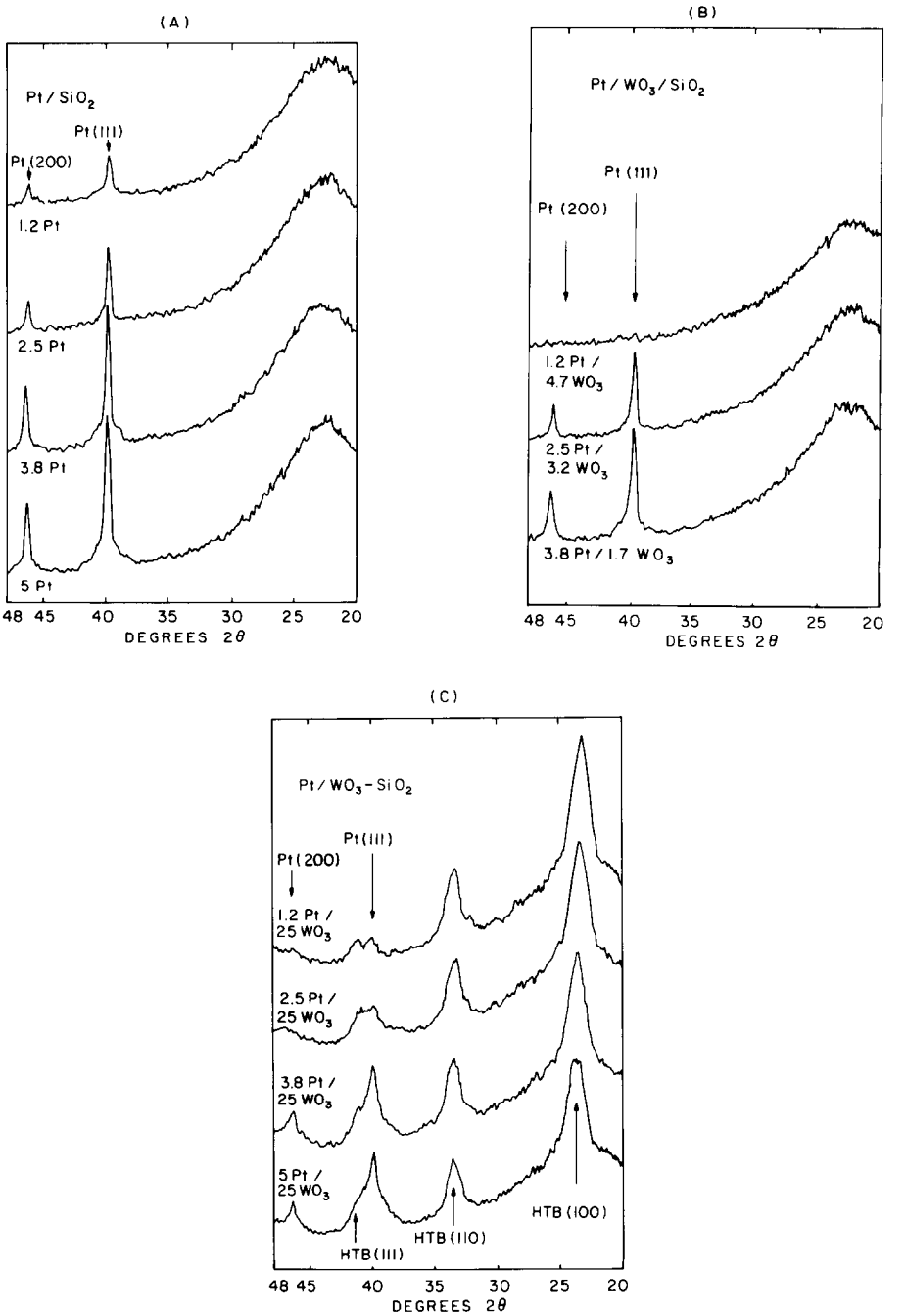

FIG. 3. XRD patterns of reduced catalysts: (A) WO_3 free, (B) low tungsta, and (C) high tungsta catalysts at various Pt loadings showing lines corresponding to Pt, WO_3, and HTB.

vealed that CO and NO species adsorb almost exclusively on Pt in the Pt/tungsta catalysts. Since CO chemisorption was selective, it was used to estimate active surface area. Plots of specific CO uptake versus weight percent Pt are shown in Fig. 4 for all WO_3 loadings. For the tungsta free catalysts, specific CO uptake decreased with increasing weight percent Pt from approximately 25 ml/g Pt for the 1.2-wt% loading to 8.7 ml/g Pt for the 5-wt% loading. Specific CO uptake decreased for the entire low tungsta series, and ranged from 11 ml/g Pt for the 1.2-wt% Pt catalyst to 7.6 ml/g Pt for the 3.8-wt% Pt catalyst. For the high tungsta series, CO uptakes once more decreased for all Pt loadings, and remained approximately constant at a value of 3.5 ml/g Pt.

Dispersion, defined as the number of surface (chemisorbing) atoms per number of total atoms is directly proportional to specific uptake and is plotted on the right-hand axis. Dispersion of surface sites appeared to decrease with increased WO_3 loading. This trend is at first peculiar, in that lower dispersion is normally associated with increased crystallite size; however, XRD analysis indicated that average crystallite size decreased with higher tungsta loadings.

Calculations of average Pt crystallite size obtained from XRD and chemisorption

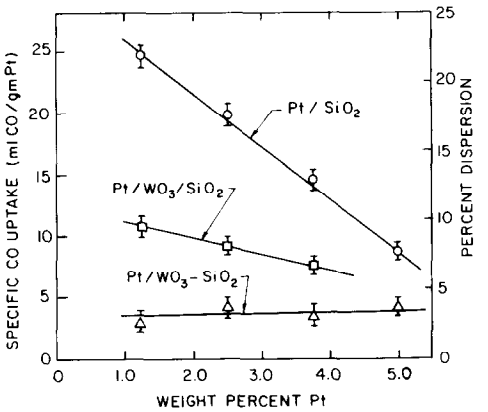

FIG. 4. Specific CO uptake and calculated dispersion for the three catalysts series versus weight percent Pt.

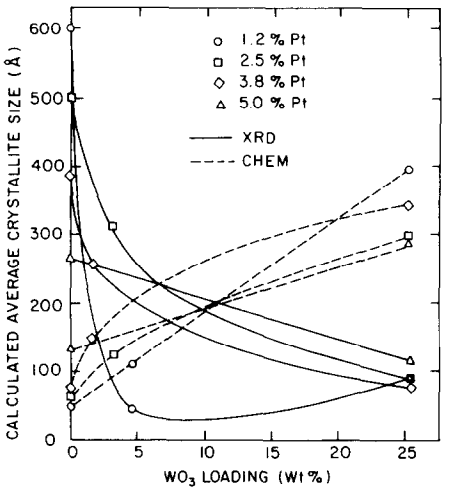

FIG. 5. Average crystallite sizes for various Pt loadings calculated from: (A) (---) chemisorption, and (B) (—) versus WO_3 loading, XRD.

measurement are contrasted in Fig. 5, and are plotted versus weight percent WO_3. For the tungsta free catalysts, XRD calculations of average crystallite size were much higher than chemisorption calculations. For the low tungsta catalysts, XRD calculations were above those for chemisorption for the 2.5 and 3.8% Pt samples, but for the 1.2% Pt catalyst the XRD estimate was below the chemisorption estimate. For all of the high tungsta catalysts, XRD estimates were below those for chemisorption. This crossover in the crystallite size calculation will be discussed later in relation to the various assumptions implicit in these two methods.

X-ray photoelectron spectroscopy. The partial reduction in WO_3 found by XRD was complemented by XPS studies as illustrated in Fig. 6 for the Pt free, high tungsta, and low and high tungsta catalyst. The lower W 4*f* peak is that of the Pt free, high tungsta catalyst, with tungsten in the fully oxidized W^{6+} (yellow WO_3) state. The spectra remained virtually unchanged up to a reduction temperature of 400°C. The upper two spectra are from representative samples of reduced Pt-containing low and high tungsta catalysts. The 400°C reduction produced W^{5+} (*28*), which created a shoulder on the low binding energy side and filled the

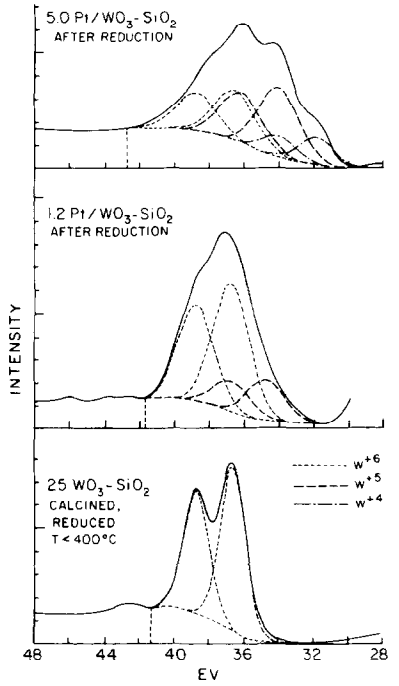

FIG. 6. XPS spectrum of the W $4f_{7/2}$ XPS line after reduction for three catalysts, showing the deconvoluted envelopes corresponding to (---) W^{6+}, (——) W^{5+}, and (·--) W^{4+}.

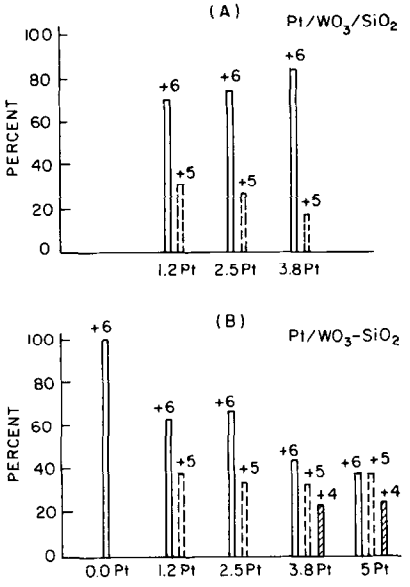

FIG. 7. Percentage of the various oxidation states of WO_3 present in (A) the low and (B) high tungsta catalysts at various Pt loadings.

valley between the $4f_{7/2}$ and $4f_{5/2}$ transitions of the W^{6+} species of the low tungsta catalyst. In addition to W^{5+}, W^{4+} (*28*) was detected for the higher Pt loadings of the high WO_3 series (top spectrum). The W $4f_{7/2}$ ebes of W^{6+}, W^{5+}, and W^{4+} were located after the curve-fitting procedure at 36.6, 34.7, and 33.6 eV, respectively, in very good agreement with the literature (*28, 40*). The support shifts the electron binding energies by about 1.1 eV toward higher values compared to the unsupported species. This effect is well known and is attributed to particle size, extra atomic relaxation changes, and increased partial charging (*28*).

The relative amounts of W^{6+}, W^{5+}, and W^{4+} were determined from the spectra in Fig. 6 and are given in Fig. 7. The extent of W^{6+} reduction appeared to depend on the loadings of both W and Pt. The percentage of W^{6+} reduced to W^{5+} in the low tungsta catalysts varied from 32% for the 1.2 Pt/4.7 WO_3/SiO_2 catalyst to 16% for the 3.8 Pt/1.7 WO_3/SiO_2 catalyst. The fraction of W^{6+} reduced in the high WO_3 series varied from 34 to 62%. The amount of W^{4+} in the 3.8 Pt/25 WO_3–SiO_2 and 5 Pt/25 WO_3–SiO_2 catalysts was calculated to be 23 and 24%.

The surface content of W, in atomic percent W, is given in Table 3. For the low tungsta series, the surface atomic percent W decreased linearly with increasing Pt loading which reflected the varying WO_3 loading in this series. There was little change upon reduction. The surface atomic percents W have been converted to weight

TABLE 3

W Surface Concentration

Catalyst	Calcined at.%	Reduced	
		at.%	wt%
1.2 Pt/4.7 WO_3/SiO_2	1.1	1.2	4.6
2.5 Pt/3.2 WO_3/SiO_2	1.0	1.0	3.9
3.8 Pt/1.7 WO_3/SiO_2	0.7	0.6	2.3
1.2 Pt/25 WO_3–SiO_2	3.0	3.4	13.1
2.5 Pt/25 WO_3–SiO_2	1.6	2.3	8.9
3.8 Pt/25 WO_3–SiO_2	1.7	1.8	7.0
5.0 Pt/25 WO_3–SiO_2	1.1	1.4	5.4

percent WO_3 so that comparison with the bulk WO_3 composition can be made. For the low tungsta series, surface weight percent WO_3 was greater than or equal to bulk weight percent indicating a good dispersion of the material.

The tungsta loading in the high tungsta series was constant, but the surface percent W monotonically decreased as the Pt loading increased. Also the high tungsta series exhibited the only consistent, appreciable change in surface percent W proceeding from calcination to reduction. The percentage consistently increased, by as much as 30% for the 2.5% Pt catalyst. By comparing the surface weight percent WO_3 (which ranged from 13.1 to 5.4 wt%) to the bulk value of 25 wt%, one sees that tungsta was not well dispersed on this catalyst series.

The presence of the $PtCl_2$ precursor, observed after calcination by XRD, was also indicated by XPS for all three catalyst series. In Fig. 8A, Pt appears mainly as Pt^{2+} at about 73 eV; however Pt° shoulders at about 71 eV are also present. The corresponding chlorine peaks are not shown. The relative amount of chlorine detected varied depending on the WO_3 loading as shown in Table 4a. The ratio of Cl to Pt in all three series was considerably less than 2 (Cl/Pt equal to 2 would be expected if all Pt was in the form of $PtCl_2$). While it decreased for both WO_3-containing catalyst series, the ratio decreased more for the low tungsta series than for the high tungsta series. Also not shown, low energy shoulders at 531 eV appeared on the oxygen 2*p* spectrum of the calcined high tungsta catalysts.

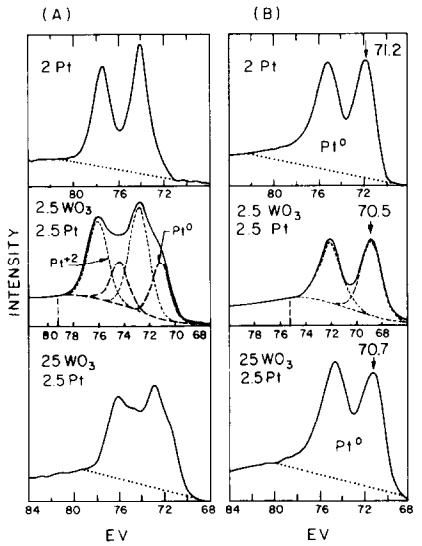

FIG. 8. XPS spectrum of Pt 4*f* electrons: (A) after calcination, (B) after reduction, for Pt tungsta free, low tungsta, and high tungsta loading catalysts.

TABLE 4a

XPS Cl/Pt Ratios

wt% Pt	WO_3 free	Low WO_3	High WO_3
1.2	1.5	trace	1.3
2.5	1.6	0.5	1.3
3.8	1.6	0.6	1.6
5.0	1.5	0.7	1.4

[a] Atomic percentage ratio.

Upon reduction (Fig. 8B) all Pt appeared present as Pt°. All chlorine peaks and the oxygen shoulders noted for the high tungsta catalysts also disappeared. The electron binding energies of the Pt $4f_{7/2}$ electrons were found to vary and are given in Table 4b. Platinum in the tungsta free catalysts exhibited a range in binding energy from 71.2 eV for 1.2 Pt/SiO_2 to 70.9 eV for 5.0 Pt/SiO_2. Some of the tungsta-containing catalysts exhibited low Pt $4f_{7.2}$ electron binding energies, the minimum being 70.5 for the 2.5 $Pt/3.2\ WO_3/SiO_2$ and 3.8 $Pt/25\ WO_3$–SiO_2 catalysts. The shift with respect to supported Pt is well outside the experimen-

TABLE 4b

Pt $4f_{7/2}$ Electron Binding Energies, Reduced Catalysts

wt% Pt	Pt $4f_{7/2}$		
	WO_3 free	Low WO_3	High WO_3
1.2	71.2	71.2	70.9
2.5	71.2	70.5	70.7
3.8	71.1	70.7	70.5
5.0	70.9	—	70.9

tal error of about ±0.1 eV. Since metallic Pt is at 71.0 eV, the negative shifts of the promoted catalysts would indicate negatively charged Pt sites.

Pt/Si ratios are plotted versus weight percent Pt for the three catalyst series in Fig. 9; these serve as an additional measure of the trend in Pt crystallite size (Pt dispersion) with tungsta loading. The ratios remained nearly constant (within 5%) proceeding from the calcination step to the reduction step, for all three series, and so only the data for the reduced catalysts are shown. The Pt/Si ratios for the tungsta free catalysts increased linearly with Pt loading, to a maximum of 1.5×10^{-2} for 5.0 Pt/SiO_2. Pt/Si ratios for the low and high tungsta catalysts also increased approximately linearly with Pt loading, but at a much higher rate than that for the tungsta free catalysts. For all but the 1.2% Pt loading, the ratios of the tungsta-containing catalysts increased by a factor of 2 to 3 over the tungsta free samples. Comparing the high and low tungsta loadings, it is seen that the Pt/Si ratios decreased from the low to the high tungsta loading, with the exception of the 1.2 Pt/25 WO_3–SiO_2 catalyst.

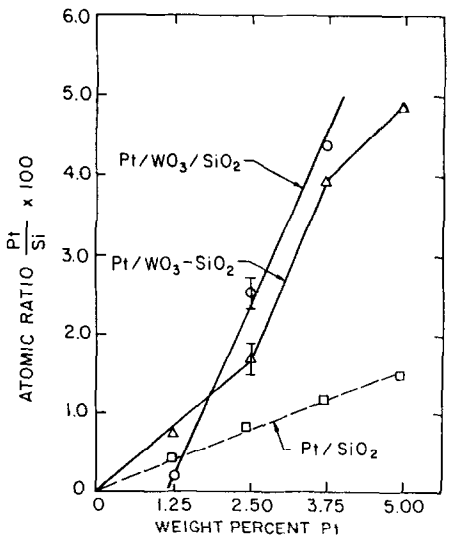

FIG. 9. Atomic Pt/Si ratios obtained from XPS data, of the three reduced catalyst series versus Pt loading.

DISCUSSION

The main characterization results can be summarized as follows:

X-ray diffraction. (i) The Pt-containing high tungsta catalysts reduced at 400°C to a black color, but produced a diffraction pattern identical to that of a blue hydrogen tungsten bronze obtained by reduction in Pt free 25 WO_3–SiO_2 at 425°C. (ii) The presence of $PtCl_2$ was detected in all catalysts after calcination and broadening of this peak increased with WO_3 loading. (iii) After reduction, Pt displayed fcc peaks which broadened with increasing WO_3 loading. Average crystallite size calculated from line broadening indicated that crystallite size decreased with WO_3 loading.

Selective chemisorption. For every Pt loading, specific CO uptake decreased with increasing WO_3 loading. Calculations based on chemisorption results indicated that average crystallite size increased with WO_3 loading in contradiction with XRD results.

XPS. (i) W^{5+} was detected in the reduced forms of both the low and the high tungsta series, and W^{4+} was detected in the high Pt, high WO_3 loadings. (ii) Pt electron binding energies in tungsta containing catalysts were slightly shifted in the negative direction relative to the WO_3 free catalysts. (iii) Chlorine/Pt ratios were lower for the tungsta-containing catalysts than for the tungsta free series. (iv) The Pt/Si ratios of the tungsta containing catalyst were two to three times higher than those of the Pt/SiO_2 catalyst, and with one exception the ratios of the low tungsta series were higher than those of the high tungsta series.

The above results are discussed below in terms of their significance in the morphology and compositions of each phase present.

The WO_3 phase. The above XRD and XPS results clearly indicate that the tungsta phase was partially reduced in the presence of Pt at a lower temperature than that in the Pt free catalysts. This confirms that Pt facilitates the partial reduction in sup-

ported tungsta, one of the hypotheses upon which this work was based. Furthermore, it appears that Pt also stabilizes the supported HTBs in the high tungsta series since they retained their color even after a 1-hr treatment in He at 400°C. This is in contrast to bulk WO_3 reduced by UV radiation in the presence of hydrogen, which was reported to revert to the fully oxidized form after exposure to air (*28*), and to a Pt/bulk WO_3 mixture stable up to 100°C (*18*).

The morphology and composition of the partially reduced trioxides can be estimated from the XPS and XRD diffraction data. For the low tungsta series, the amount of W^{5+} relative to W^{6+} (Fig. 7) ranged from 16 to 30%. Additionally, the suboxides were well dispersed as previously noted (Table 3). They existed as very thin layers of HTBs of compositions $H_{0.1}WO_3$ and $H_{0.33}WO_3$ or if the hydrogen was eliminated as water, the resulting anhydrous suboxides would have compositions ranging from $WO_{2.7}$–$WO_{2.84}$.

The dispersion of tungsta in the high tungsta series was much worse than that in the low tungsta series. The surface weight percents (Table 3), which ranged from 13.1 to 5.4, are below the monolayer breakpoint of 23.2 wt%. Some well-dispersed material likely coexists with the bulk WO_3, but there is far less than a monolayer of it. The calcination temperature of 700°C was 150°C higher than that used in the study in which the breakpoint value was reported (*14*), causing some sintering, thus leading to the formation of both well-dispersed and bulk WO_3.

The reduced high tungsta catalysts are therefore thought to contain a high fraction of bulk HTB. HTB composition can be estimated from XPS. However, in the case of the high tungsta loading similar estimates based on XPS compositions including W^{4+} yields values of x for H_xWO_3 species of about 0.8 and 0.9 for the 3.8 Pt/25 WO_3–SiO_2 and 5.0 Pt/25 WO_3–SiO_2 catalysts. These values of x are too high since the maximum stoichiometry of the H_xWO_3 is known to be $x = 0.5$ (*17, 18*). It has been shown in the literature that H_xWO_3 phases contain only W^{5+} but not W^{4+} (*28*). Therefore if W^{4+} is assumed to form a separate phase and x is estimated from the fractions of W^{6+} and W^{5+} phases, then the values of x range from 0.34 to 0.5. These correspond very well to the compositions of $H_{0.33}WO_3$–$H_{0.5}WO_3$ found from XRD. W^{4+} was observable by XPS but not XRD, which revealed only HTB: consequently the species containing W^{4+}, likely WO_2, must be amorphous or close to the surface relative to the HTB.

The formation of a separate W^{4+} phase attributable to WO_2 also explains the chromatic effects observable. The black coloration of the high tungsta catalysts would result from dark brown WO_2 and the dark blue HTB.

The Pt phase. An issue that needs to be addressed is the effect of WO_3 on Pt crystallite size and the discrepancy between XRD and CO chemisorption results. The crystallite size effect is in part related to the $PtCl_2$ phase detected by XRD and XPS, after the calcination step. Clearly not all the Pt is in this phase, as XPS Cl/Pt ratios were less than 2 and the Pt spectra (Fig. 9) indicate the presence of some zero valence Pt. But because the $PtCl_2$ peaks broadened and the Cl/Pt ratios decreased for the tungsta-containing catalysts, it appears that less bulk $PtCl_2$ formed. It has been demonstrated that a $PtCl_2$ precursor increases Pt crystallite size (*30, 31*). It is interesting to note that the Cl/Pt ratios of the high tungsta series are greater than those for the low tungsta series. It is speculated that at the higher tungsta loading a more dispersed oxychloroplatinate precursor formed. The observation of precursor oxygen binding energy shoulders for only this series supports this explanation.

The trend in the $PtCl_2$ effect on crystallite size thus parallels average crystallite size calculations based on broadening of the Pt(111) line, which indicate that crystallite size decreased with increasing WO_3 loading

(with the exception of the 1.2 Pt/25 WO_3–SiO_2 catalyst). However, chemisorption estimates of average crystallite size differ from XRD not only in the magnitude but also in the trend with WO_3 loading (Fig. 6). For the Pt free catalysts, XRD estimates are higher than chemisorption estimates. This case is commonly encountered when crystallites with sizes below the 50-Å limit of XRD, but detectable by chemisorption, are present. However, with the high WO_3 loading catalysts, the trend reverses, i.e., chemisorption estimates are higher than XRD calculations. This indicates that chemisorption is insufficient to account for the Pt surface area conservatively detected by XRD, and reveals that chemisorption suppression occurs with the addition of WO_3.

The Pt–WO_x phase. Chemisorption supression can occur if a partially reduced oxide is decorating the surface of the active metal by blocking chemisorption sites. Such a model is now well established in the literature for many SMSI systems. In the case in point partially reduced WO_3 oxides such as WO_2, detected by XPS and shown to be surface localized, would be decorating the Pt surface.

A second way in which the presence of a decorating species can be ascertained is by examination of Pt/Si (metal/support) ratios from the XPS data. These data can be used as an additional measure of metal dispersion. The Pt/Si ratio can represent an additional measure of metal dispersion provided that the support signal remains constant (*32*). If part of the Si signal is eliminated by either Pt or W covering Si sites, then the signal would have been attenuated at most 3.4% by W (Table 3) and 4.8% by Pt (Fig. 9). Because decreasing Pt crystallite size with increasing tungsta loading is evidenced by X-ray diffraction, the Pt/Si signal for any individual Pt loading might be expected to increase in the order

$$Pt/SiO_2 < Pt/\text{low } WO_3/SiO_2 < Pt/\text{high } WO_3\text{–}SiO_2.$$

However, after increasing from the tungsta free to the low tungsta series, Pt/Si ratios generally decrease from the low to the high loading (Fig. 9). That is, the observed trend in Pt/Si ratios is

$$Pt/SiO_2 < Pt/\text{high } WO_3\text{–}SiO_2 < Pt/\text{low } WO_3/SiO_2.$$

Such a decrease in Pt signal with decreasing Pt crystallite size can be accounted for only by decoration; even though Pt crystallites were smallest (exhibited the most Pt surface) for the high tungsta catalysts, some of the Pt XPS signal must have been blocked by decorating species. In other words this means that the exposed Pt surface area is les than the total amount of Pt area.

Thus XPS Pt/Si ratios support a morphological model of decreased Pt crystallite size accompanied by increased decoration, as tungsta loading, is increased. It is postulated that at first, with low tungsta loading, the crystallite size effect predominates in the XPS data, while for higher tungsta loading, the decoration effect becomes apparent. Increased decoration for the high tungsta series relative to the low tungsta series is also supported by Fig. 8, which shows that W^{6+} in the high tungsta catalysts was reduced to a greater extent than in the low tungsta catalysts. However, XPS data cannot be used to estimate the absolute extent of decoration. Chemisorption results indicated that both tungsta-containing catalyst series had less active Pt surface area than the tungsta free catalysts. The fact that the decoration effect did not dominate more for both series could very well have been because the layers decorating Pt crystallites were thick enough to block chemisorption, but not thick enough to completely block the Pt XPS signal (meaning that they were probably much less than 20 Å thick).

The catalyst 1.2 Pt/25 WO_3–SiO_2 shows an increased Pt crystallite size from XRD (Fig. 3) and XPS Pt/Si ratios (Fig. 9) which deviates from the trends followed by the

other catalysts. In this catalyst the tungsta loading was sufficiently high to fill small pores (see BET data) which prevented the formation of small Pt crystallites in those pores, thus resulting in lower dispersion. The Pt loadings in the other high tungsta catalysts series were higher, leading to the formation of larger crystallites and thus were not adversely affected by pore filling. In the low tungsta series, pore filling was not significant, thus the presence of tungsta increases dispersion by interacting with the $PtCl_2$ precursor. Such an effect did not occur in the Pt/SiO_2 tungsta free catalysts.

Another result that supports a decoration model is the small but noticeable negative shift in the Pt $4f_{7/2}$ binding energies observed with increased WO_3 loading. Normally binding energy shifts of supported noble metals are positive due to either an increase in oxidation state or changes in extraatomic relaxation for very small metal particles. Negative shifts of electron binding energies for Pd on Pd/La_2O_3 catalysts have been recently reported in conjunction with support decoration (*33–35*). Partial negative charges on Pd were ascribed to charge transfer to Pd from patches of partially reduced La oxide on top of Pd crystallites. Partial negative charges on Pt might result from electron transfer from partially reduced tungsta oxides. Recent experimental and theoretical data (*36–39*) show that *d*-electrons from a partially reduced transition metal oxide can be transferred to the *d*-band of the metal crystallite. Such a charge transfer to Pd or Pt will lead to a nearly full 4*d*- or 5*d*-band, respectively, which moves Pt and Pd electronically closer to their Group IB neighbors, Ag and Au. The latter do not chemisorb CO. Electron transfer might also arise from the bulk HTB; lattice hydrogen contributes electrons to the HTB conduction band (*18*). Tungsta in HTB is present as W^{5+} with the electronic structure [Xe] $4f^{14}5d^1$ and an interaction of the lone 5*d* electron with Pt[Xe] $4f^{14}5d^96s^1$ is certainly conceivable. These negative shifts differ from characterization of $Pt/MoO_3/Al_2O_3$ catalysts (*5*), in which electronic interactions were postulated to occur between Pt and partially reduced Mo ions, but Pt in the reduced state exhibited positive binding energy shifts. A possible explanation of the difference is that the Pt post-calcination precursor state in the Pt/MoO_3 catalysts was PtO_2, different from the $PtCl_2$ form observed in this work.

The morphology of the Pt/WO_3–SiO_2 catalysts. On the basis of the above discussion, the results obtained are consistent with a model of the surface containing small and large Pt crystallites both located on the silica support and on the WO_3 phase. Pt located on the tungsta phase decreased the difficulty of reducing tungsta, leading to the formation of HTB and tungsta suboxides. WO_3 in turn affected the Pt crystallite size in part by decreasing the amount and size of bulk $PtCl_2$ crystallites formed after post calcination. Tungsta suboxides, such as WO_2, form a separate phase from HTB, and decorate the surface of the reduced Pt thus decreasing CO chemisorption. A schematic representation of a model surface with main characteristics consistent with those indicated by the experimental work is shown in Fig. 10.

Further support for the above model has been obtained from TEM studies of model $Pt/WO_3/SiO_2$ catalysts, to be presented in part II of this work, and from an FTIR and kinetic investigation of the NO–CO reaction over these catalysts. The latter study, to be presented in part III, also demonstrates that the decorating species lead to an increased activity characteristic of the SMSI state.

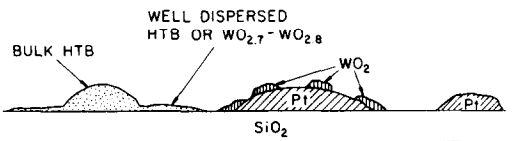

FIG. 10. Schematic representation of the most probable morphological configuration of the various phases on the supported catalysts.

REFERENCES

1. Liao, P. C., Carberry, J. J., Fleisch, T., and Wolf, E. E., *J. Catal.* **74,** 307 (1982).
2. Liao, P. C., Fleisch, T., and Wolf, E. E., *J. Catal.* **75,** 396 (1982).
3. Varghese, P., and Wolf, E. E., *AIChE Symp. Ser.* **201,** 195 (1980).
4. Gandhi, H. S., Yao, H. C., and Stepien, H. K., *ACS Symp. Ser.* **178,** 143 (1982).
5. Devries, J. E., Yao, H. C., Baird, R. J., and Gandhi, H. S., *J. Catal.* **84,** 1983, 8.
6. Yao, H. C., Rothschild, W. G., and Gandhi, H. S., *in* "Catalysis on the Energy Scene" (S. Kaliaguine, and A. Mahay, Eds.). Elsevier, Amsterdam, 1984.
7. Adams, K. M., and Gandhi, H. S., *Ind. Eng. Chem. Prod. Res. Dev.* **22,** 207 (1983).
8. Plummer, H. K., Jr., Shinozaki, S., Adams, K. M., and Gandhi, H. S., *J. Mol. Catal.* **20,** 251 (1983).
9. Yates, J. T., Jr., and Madey, T. E., *J. Chem. Phys.* **4**(5), 1623 (1966).
10. Masel, R. I., Umbach, E., Fuggle, J. C., and D. Menzel, *Surf. Sci.* **79,** 26 (1979).
11. Sato, M., *Surf. Sci.* **95,** 269 (1980).
12. Egelhoff, W. F., Jr., *in* "The Chemical Physics of Solid Surfaces and Heterogeneous Catalysis" (D. A. King, and D. P. Woodruf, Eds.). Elsevier, New York, 1982.
13. Biloen, P., and Pott, G. T., *J. Catal.* **30,** 169 (1973).
14. Thomas, R., Van Oers, E. M., DeBeer, V. H., and Moulijn, J. A., *J. Catal.* **84,** 275 (1983).
15. Boudart, M., Vannice, M. A., and Benson, J. E., *Z. Phys. Chem. Neue Folge* **64,** 171 (1969).
16. Benson, J. E., Kohn, H. W., and Boudart, M., *J. Catal.* **5,** 307 (1966).
17. Sermon, P. A., and Bond, G. C., *Catal. Rev.* **8**(2), 211 (1973).
18. Sermon, P. A., and Bond, G. C., *J. Chem. Soc. Faraday Trans. 1* **72,** 730 (1976).
19. Tauster, S. J., *ACS Symp. Ser.* **298,** 1 (1986).
20. Murrell, L. L., Dispenziere, N. C., Jr., Baker, R. T. K., and Chludzinski, J. J., *ACS Symp. Ser.* **298,** 195 (1986).
21. Regalbuto, J. R., and Wolf, E. E., *J. Catal.*, in press.
22. Regalbuto, J. R., and Wolf, E. E., *J. Catal.*, in press.
23. Regalbuto, J. R., Ph.D. thesis, University of Notre Dame, 1986.
24. Pande, N. K., and Bell, A. T., *Appl. catal.* **20,** 109 (1986).
25. Pande, N. K., and Bell, A. T., *J. Catal.* **97,** 137 (1986).
26. McVicker, G. B., and Ziemiak, J. J., *J. Catal.* **95,** 473 (1985).
27. Jun-Ying, Y., and Swartz, W. E., Jr., *Spectrosc. Lett.* **17**(6–7), 331 (1984).
28. Fleisch, T. H., and Mains, G. J., *J. Chem. Phys.* **76**(2), 780 (1982).
29. Glemser, O., and Naumann, C., *Z. Anorg. Allgem. Chem.* **265,** 288 (1951).
30. Foger, K., and Jaeger, H., *J. Catal.* **92,** 64 (1985).
31. Jenkins, J. W., "Prepr. 6th Canad. Symp. Catal. Ottawa, 1979," p. 21.
32. Hercules, D. M., *Trends Anal. Chem.* **3**(5), 125 (1984).
33. Fleisch, T. H., Hicks, R. T., and Bell, A. T., *J. Catal.* **87,** 398 (1984).
34. Ermakov, Y. I., Kuznetsov, B. N., Ryndin, Y. A., and Duplyakin, V. K., *Kinet. Katal.* **15**(4), 1093 (1974).
35. Hicks, R. F., Yen, Q. J., Bell, A. T., and Fleisch, T. H., *Appl. Surf. Sci.* **19,** 315 (1984).
36. Hermann, J. M., *J. Catal.* **89,** 404 (1984).
37. Kao, C. C., Tsai, S. C., and Chung, Y. W., *J. Catal.* **73,** 136 (1982).
38. Fung, S. C., *J. Catal.* **76,** 225 (1982).
39. Horsley, *J. Amer. Chem. Soc.* **101,** 2870 (1979).
40. Wagner, C. D., Riggs, W. M., Davis, L. E., Moulder, J. F., and Muilenberg, G. E., "Handbook of XPS." Perkin–Elmer, Palo Alto, CA, 1979.